PHYSICAL SCIENCES

Simultaneous multitone microwave emission by dc-driven spintronic nano-element

Alexandre Abbass Hamadeh[1]*, Denys Slobodianiuk[2,3], Rayan Moukhader[4], Gennadiy Melkov[2], Vladyslav Borynskyi[3], Morteza Mohseni[1], Giovanni Finocchio[4], Vitaly Lomakin[5], Roman Verba[3], Grégoire de Loubens[6], Philipp Pirro[1], Olivier Klein[7]

Current-induced self-sustained magnetization oscillations in spin-torque nano-oscillators (STNOs) are promising candidates for ultra-agile microwave sources or detectors. While usually STNOs behave as a monochromatic source, we report here clear bimodal simultaneous emission of incommensurate microwave oscillations in the frequency range of 6 to 10 gigahertz at femtowatt level power. These two tones correspond to two parametrically coupled eigenmodes with tunable splitting. The emission range is crucially sensitive to the change in hybridization of the eigenmodes of free and fixed layers, for instance, through a slight tilt of the applied magnetic field from the normal of the nanopillar. Our experimental findings are supported both analytically and by micromagnetic simulations, which ascribe the process to four-magnon scattering between a pair of radially symmetric magnon modes and a pair of magnon modes with opposite azimuthal index. Our findings pave the way for enhanced cognitive telecommunications and neuromorphic systems that use frequency multiplexing to improve communication performance.

INTRODUCTION

A great number of research projects have been devoted to the study of spin transfer torque (STT) after its theoretical prediction (*1*, *2*). This new paradigm is meant to ignite a conceptual metamorphosis of spintronics, a research field which capitalizes on the spin degree of freedom of the electron (*3*). The STT effect can enable a variety of spintronics applications, such as spin-torque magnetic random access memories (*4*) and spin-torque nano-oscillators (STNOs) (*5*). The use of STNOs to generate microwave signals in nanoscale devices has generated tremendous and continuous research interest in recent years (*6*–*11*). Their key features are frequency tunability (*12*), nanoscale size (*10*), broad working temperature (*13*), and easy integration with the standard silicon technology (*6*, *14*). As strongly nonlinear devices, STNOs can exhibit different dynamic regimes, which are promising candidates for various applications including microwave signal generation and detection (*15*–*17*), signal modulation (*18*), spin wave generation (*19*), neuromorphic computing (*20*–*22*), etc.

In general, only a single mode is expected to oscillate at one time in an STNO as predicted by the universal oscillator model (*23*). Multimodal cogeneration of weak commensurate tones can be produced by harmonic distortion. Here, the tones are intrinsically linked by rational numbers. Alternatively, mode hopping between nearly degenerate eigen-solutions have been reported (*24*–*26*) induced by thermal fluctuations (*27*), spatial inhomogeneity of the internal field in asymmetric ferromagnetic bilayers (*28*), or by formation of higher-order modes of excited magnetic solitons (*29*). Also, a high level of thermal fluctuations can result in a seemingly multimode generation that is just an amplification of the incoherent thermal population of higher modes.

In this study, we find and elucidate another possibility to create stable simultaneous excitation of multiple spin wave modes in an STNO with a continuously adjustable splitting. The leading order mechanism supporting multimode generation is found to be four-magnon scattering or, in other words, second-order parametric instability. Although this process is well-known in magnetic systems (*30*–*33*), its observation in an STNO is often prohibited as it is impossible to satisfy both energy and angular momentum conservation rules simultaneously. We found that parametric instability becomes possible because of strong hybridization between the modes of the two layers of the STNO, which also makes the parametric process highly sensitive to external conditions and thus controllable.

RESULTS

Bimodal generation in STNO

The studied STNO is a circular nanopillar with a diameter of 250 nm, consisting of (Cu60|Py15|Cu10|Py4|Au25) layers where the Py (Permalloy) is composed of $Ni_{80}Fe_{20}$. The numbers indicate the thickness in nanometers. This structure was designed using electron beam lithography, and the top and bottom Au and Cu electrodes were specifically tailored for microwave transport measurements. The STNO is excited by a negative dc current I_{dc}, corresponding to an electron flow from the thin to the thick magnetic layer, which allows us to observe STT-induced microwave generation. In the measurements presented below, a bias magnetic field in the range $H_{ext} \in [8.5, 9.6]$ kOe was applied at $\theta_H = 2°$ from the sample normal (see Fig. 1A). This tilt is introduced to create a small misalignment between the static magnetizations of the layers, which is required for the appearance of resistance (and voltage)

[1]Fachbereich Physik and Landesforschungszentrum OPTIMAS, Rheinland-Pfälzische Technische Universität Kaiserslautern-Landau, 67663 Kaiserslautern, Germany. [2]Taras Shevchenko National University of Kyiv, Kyiv 01601, Ukraine. [3]Institute of Magnetism, Kyiv 03142, Ukraine. [4]Department of Mathematical and Computer Sciences, Physical Sciences and Earth Sciences, University of Messina, 98166 Messina, Italy. [5]Center for Magnetic Recording Research, University of California San Diego, La Jolla, CA 92093-0401, USA. [6]SPEC, CEA, CNRS, Université Paris-Saclay, 91191 Gif-sur-Yvette, France. [7]Univ. Grenoble Alpes, CEA, CNRS, Grenoble INP, Spintec, 38054 Grenoble, France.
*Corresponding author. Email: hamadeh@rptu.de

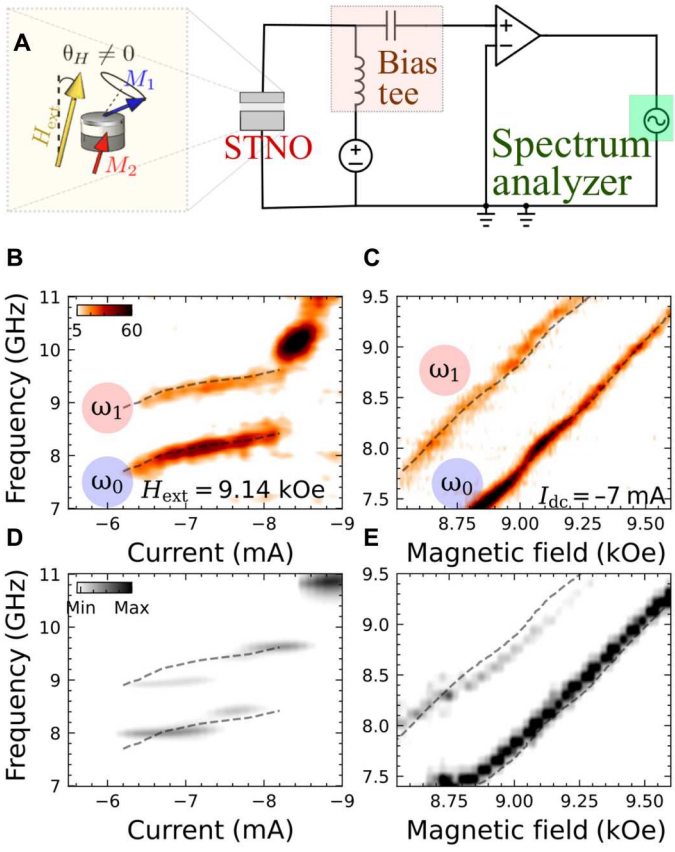

Fig. 1. Characterization of microwave generation in STNO under different conditions. (**A**) Experimental setup for electrical measurement. (**B**) Dependence of the microwave generation characteristics of the STNO on the dc current at constant bias field H_{ext} = 9.14 kOe and (**C**) on the external field at a fixed dc current I = −7 mA; [(B) and (C)] experiment and [(D) and (E)] micromagnetic simulations showing the oscillations of two modes simultaneously. Dashed lines show the location of the oscillation modes in the experiment, and the intensity scale indicates the normalized power (in fW/GHz for the experimental data).

oscillations under almost circular magnetization precession; in the case of $\theta_H = 0°$ voltage oscillations vanish (*34*). However, this symmetry breaking also has substantial consequences on the entire dynamics, as discussed in the following.

First, the bias current dependence of the voltage oscillation spectra under a constant magnetic field H_{ext} = 9.14 kOe is reported in Fig. 1B. Within the current range from −6 to −8 mA, we observe two simultaneously auto-oscillating modes, referred below as ω_0 and ω_1, which are split by about 1.1 GHz. With a further current increase, the generation frequency exhibits a pronounced jump and generation becomes seemingly single-mode (the second mode is hardly detectable). Also, this jump is accompanied by a substantial power increase (see the intensity scale and the Supplementary Materials). At even higher currents, the STNO generation demonstrates further frequency jumps and complex dynamics that are not considered here. Within the bimodal regime at $I_{dc} \in [-6, -8.2]$ mA, the frequencies of both modes demonstrate the same weak increase with the current amplitude, which is unexpected for almost perpendicularly magnetized STNO, characterized by a strong nonlinear frequency shift (*23*).

Figure 1C presents the frequency evolution with the strength of a magnetic field under a constant dc current I_{dc} = −7 mA. The bimodal regime is robust to the field strength variation and is observed in the entire presented field range. The frequencies of both oscillation modes ω_0 and ω_1 vary almost linearly with the applied field; in almost perpendicularly magnetized STNO, such dependence is not trivial as it may appear, indicating a substantial nonlinear damping effect (*23*). It is worth noting that in the case of perpendicular magnetization ($\theta_H = 0°$), the generation characteristics of the STNO become fairly standard, and none of the features described here indicating bimodal generation were observed (*34*).

Micromagnetic simulations: Autonomous dynamics and mode hybridization

To get a deeper insight into the magnetization dynamics, micromagnetic simulations were performed using the FastMag software package (*35*) that is based on the finite elements method (FEM). FastMag allows computing the full system including interactions between the reference and free layer via mutual STT effects. FastMag also calculates the magneto-resistance response that can be directly compared to the experimental measurements. Material parameters were taken from the experimental study of passive dynamics (i.e., below auto-oscillation threshold) of the nanopillar (*36*) (see details in Methods). The FEM mesh edge length was chosen as 2.6 nm. The data evaluation of simulation was done through Aithericon (see www.aithericon.com for further information and details).

To excite the oscillation dynamics, a negative dc current was applied through the structure. The results of these micromagnetic simulations, shown in Fig. 1 (D and E), reproduce the experimental measurements with a good qualitative and quantitative agreement, a clear indication that the advanced micromagnetic modeling is able to capture the features leading to the observed complex behavior. Reference simulations performed for the case $\theta_H = 0°$ show standard single-mode STNO behavior, in accordance with a previous experimental study (*34*).

Next, we investigate spectra of the magnetization dynamics by evaluating the fast Fourier transform (FFT) of the circularly polarized transverse magnetization components $M_+ = M_x + iM_y$ emitted by the electrically driven STNO, where i is the imaginary unit. In contrast to the resistance oscillation spectra, they demonstrate three peaks—an additional peak, referred to as ω_2, is visible below ω_0 (Fig. 2A). The frequencies of the peaks satisfy the relation $2\omega_0 = \omega_1 + \omega_2$, which leads us to the assumption that four-magnon interaction between these modes, schematically shown in Fig. 2B, is involved in STNO dynamics. Using a mesh resolved FFT, we obtain the spatial profiles of the excitations corresponding to these peaks. The main mode ω_0 is a quasi-uniform mode characterized by respectively a radial index m = 0 and an azimuthal index ℓ = 0, which we label (m = 0, ℓ = 0) mode. This mode can be identified as the lowest-frequency mode of the free layer. The peak at ω_1 is the (0, −1) azimuthal mode, also mostly localized within the free layer. The excitation at ω_2 resembles the (0, +1) azimuthal mode. However, in contrast to other excitations, this mode has comparable oscillation amplitude in both thin and thick STNO layers indicating a strong hybridization.

To elucidate the nature of the signal at ω_2, we performed micromagnetic simulations of the STNO modes in the passive regime (no dc current) (see Methods). We found that in our device, the $\ell = \pm 1$ azimuthal eigenmodes of the thick layer are located below the

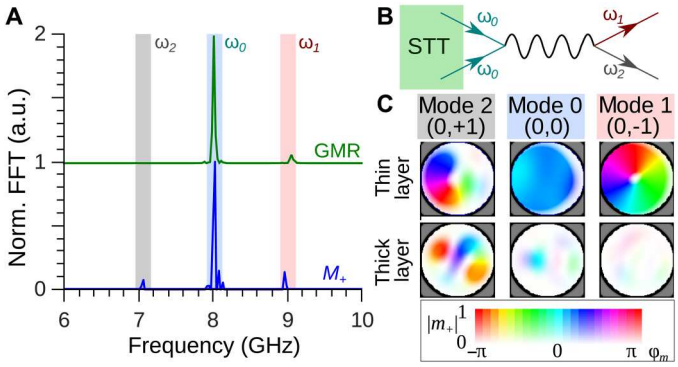

Fig. 2. Analysis of STNO's magnetization spectrum, scattering process, and precession profiles. (**A**) Frequency spectrum of the M_+ magnetization component (blue line) and spectrum of the magnetoresistance oscillations (green line, vertically offset) of the STNO under a bias current $I_{dc} = -7$ mA, obtained by micromagnetic simulations; in arbitrary units (a.u.). (**B**) A diagram illustrating the four-magnon scattering process leading to the multimode generation in the STNO. (**C**) Spatially resolved magnetization precession patterns of the three modes, obtained via FFT of magnetization time traces. The brightness indicates the amplitude, and the hue indicates the phase.

fundamental mode of the thin layer (because of different saturation magnetization), and these modes experience strong hybridization so that the oscillation amplitude is comparable in both layers (Fig. 3B). The last fact explains why the mode at ω_2 is not visible in giant magnetoresistance (GMR) spectra: the relative angle between the layers magnetizations is only weakly changed when it is excited. Thus, we attribute the multimode generation to a four-magnon process involving the fundamental mode (0,0) of the thin layer, the azimuthal (0, −1) mode of the thin layer and the (0, +1) mode of the thick layer that is strongly hybridized to the thin layer. This process satisfies the momentum conservation rule $2\ell_0 = \ell_1 + \ell_2$, and the mode eigenfrequencies are reasonably close to the energy conservation rule $2\omega_0 = \omega_1 + \omega_2$. An additional check that the thick layer mode is involved in the multimode generation was made by simulating the active STNO with a drastically increased local field in the thick layer. In this case, the thick layer modes are shifted to much higher frequencies and the abovementioned four-magnon process becomes impossible. No multimode generation was observed in this case. In the reference case of a perpendicular

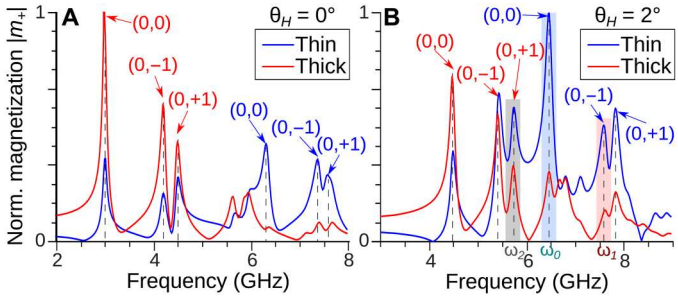

Fig. 3. Hybridized eigenmodes of two-layer oscillations. Spectra of linear (low-amplitude) magnetization oscillations of the STNO nanopillar, excited by spatially nonuniform magnetic field (micromagnetic simulations); the modulus of averaged in a quarter of thin and thick layers dynamic magnetization m_+, normalized to maximal value, is shown.

field, the thick layer modes shift to lower frequencies and thus experience much less hybridization (Fig. 3A), which is crucial for the multimode generation as discussed below.

Analytical model of STNO dynamics with parametric intermode coupling

In the following, we consider an analytical model to describe the dynamics of STNO modes including parametric coupling. As before, we denote the fundamental mode as mode "0" having the amplitude a_0, the (0, −1) mode of the thin layer and (0, +1) thick layer mode as modes 1 and 2, respectively, and consider dynamics of only these three modes. The mentioned four-magnon process is described by the term $\mathcal{H}^{(4)} = W_{00,12} a_1 a_2 a_0^* a_0^* + \text{c.c.}$ in the Hamiltonian of the system. Taking it into account, the dynamics of the coupled modes is described by equations

$$\begin{aligned} \dot{a}_0 + i\tilde{\omega}_0 a_0 + \tilde{\Gamma}_0 a_0 &= -2iW_{00,12} a_0^* a_1 a_2 \\ \dot{a}_1 + i\tilde{\omega}_1 a_1 + \tilde{\Gamma}_1 a_1 &= -iW_{00,12}^* a_0^2 a_2^* \\ \dot{a}_2 + i\tilde{\omega}_2 a_2 + \tilde{\Gamma}_2 a_2 &= -iW_{00,12}^* a_0^2 a_1^* \end{aligned} \quad (1)$$

Here, an overdot denotes time derivative, $\dot{a} = \partial_t a$, and $\tilde{\omega}_i$ and $\tilde{\Gamma}_i$ are frequency and total damping of ith mode accounting for nonlinear contributions. In a general case, "total" frequency includes linear eigenfrequency and self- and cross-nonlinear shifts from all modes: $\tilde{\omega}_i = \omega_i + T_i|a_i|^2 + 2\sum_{j\neq i} T_{ij}|a_j|^2$. The total damping accounts for nonlinear changes of both the damping and the STT anti-damping torque (*23*): $\tilde{\Gamma}_i = \Gamma_i(1 + \xi_i|a_i|^2 + 2\sum_{j\neq i}\xi_{ij}|a_j|^2) - \sigma_i I(1 - \tilde{\xi}_i|a_i|^2 - 2\sum_{j\neq i}\tilde{\xi}_{ij}|a_j|^2)$, where $\Gamma_i = \alpha_G\omega_i$ is the linear Gilbert damping, σ is the STT efficiency, and $\tilde{\xi}_{ij}$ are the nonlinear coefficients (see Methods).

Since the energy of mode 2 is more concentrated in the thick layer, while modes 0 and 1 are concentrated in the thin one, we neglect all related frequency and damping cross shifts, such as $T_{i2} = 0$, $\xi_{i2} = 0$, etc. Only for the STT term ($\tilde{\xi}_{2i}$), such simplification is not appropriate since it is inversely proportional to the layer thickness, so the thin layer contribution to the total STT could be dominant even for mode 2. Linear frequencies for the model were extracted from micromagnetic data, and nonlinear coefficients were estimated using the vector Hamiltonian formalism (*37*, *38*), as described in Methods.

When the current increases, mode 0 first turns to the self-oscillation regime; this happens at $I_{th} = \Gamma_0/\sigma$ (corresponding to −6 mA in the experiment). Formal thresholds of "isolated" modes 1 and 2 Γ_i/σ_i are larger, but the competition for common STT pumping prohibits excitation of higher-order modes above their formal thresholds in the absence of other coupling (*27*), and the only source for their excitation is the parametric instability of the mode 0. Then, assuming negligible amplitudes of the modes 1 and 2, we can calculate the "virtual" amplitude of mode 0 above the threshold in the absence of other modes, $|a_0|^2 = (\sigma I - \Gamma_0)/[\xi_0(\sigma I - \Gamma_0)]$ (*23*), and the threshold amplitude a_{th} of mode 0, above which parametric instability develops (*38*)

$$|a_{th}|^2 = \frac{\sqrt{\tilde{\Gamma}_1\tilde{\Gamma}_2}}{|W_{00,12}|}\sqrt{1 + \frac{(2\tilde{\omega}_0 - \tilde{\omega}_1 - \tilde{\omega}_2)^2}{(\tilde{\Gamma}_1 + \tilde{\Gamma}_2)^2}} \quad (2)$$

Here, the nonlinear frequency and the damping are calculated for the free-running amplitude of mode 0 at a given current and

vanishing amplitudes of other modes. If $|a_0| > |a_{th}|$, then the parametric instability occurs, and modes 1 and 2 are excited.

Dependencies of the isolated free-running amplitude a_0 and the parametric instability threshold are shown in Fig. 4 (A and B), right axis. In the case of $\theta_H = 2°$, the threshold is overcome in a certain range of currents, and a three-mode generation is expected. In contrast, in the reference case of a perpendicular field, the instability threshold is never overcome, and single-mode generation is expected. There are two reasons for this difference. The first one is the larger detuning from exact parametric resonance $\Delta\omega = 2\tilde{\omega}_0 - \tilde{\omega}_1 - \tilde{\omega}_2$ [see Fig. 4 (A and B)] because of the different positions of the thick layer eigenmodes. However, this difference is not drastic, and the second reason, namely, the notably (threefold) reduced parametric coupling $W_{00,12}$ also plays a crucial role. The latter is a result of the much lower hybridization of the modes, which is clear from the comparison of the oscillation amplitude in the thin layer at the position of (0, +1) mode of the thick layer in Fig. 3 (see calculation details in Methods). The same reason determines the explanation for the observation of this particular pair of parametric modes at $\theta_H = 2°$. Another pair, which also satisfies the momentum conservation [(0, −1) thick layer mode and (0, +1) thin layer mode], exhibits smaller parametric coupling because of lower hybridization of the (0, −1) thick layer mode (Fig. 3B).

Last, we numerically integrate Eq. 1 and present the stationary mode frequencies and amplitudes in Fig. 4C. Starting from the threshold $\sigma I = \Gamma_0$, the amplitude and frequency of the mode 0 increase and reach the parametric instability threshold ($\sigma I/\Gamma_0 \approx 1.035$). Above this instability threshold, all three modes are excited, and their frequencies are almost frozen (a feature that could be interesting for certain applications). In this regime, the parametric process dominates, and the modes have stationary amplitudes that almost satisfy the parametric resonance condition $2\tilde{\omega}_0(a_i) \approx \tilde{\omega}_1(a_i) + \tilde{\omega}_2(a_i)$. Above $\sigma I/\Gamma_0 \approx 1.18$, this generation regime cannot be sustained anymore, and we observed an abrupt jump of the mode frequencies and amplitudes as discerned in the experiment (see Fig. 1B). Mode 0 acquires an amplitude and a frequency that are close to the ones in the absence of parametric pumping, while modes 1 and 2 oscillate far from their "nonlinear eigenfrequencies" (i.e., the parametric process becomes strongly nonresonant). Their amplitudes decrease up to the current $\sigma I/\Gamma_0 \approx 1.36$, above which the instability threshold becomes too high and the STNO returns to single-mode regime. Within the multimode generation range, the amplitude of parametric mode 1 is evidently larger than of the mode 2. This can be attributed to the substantially larger total damping rate of the mode 2. This circumstance also complicates the experimental observation of mode 2.

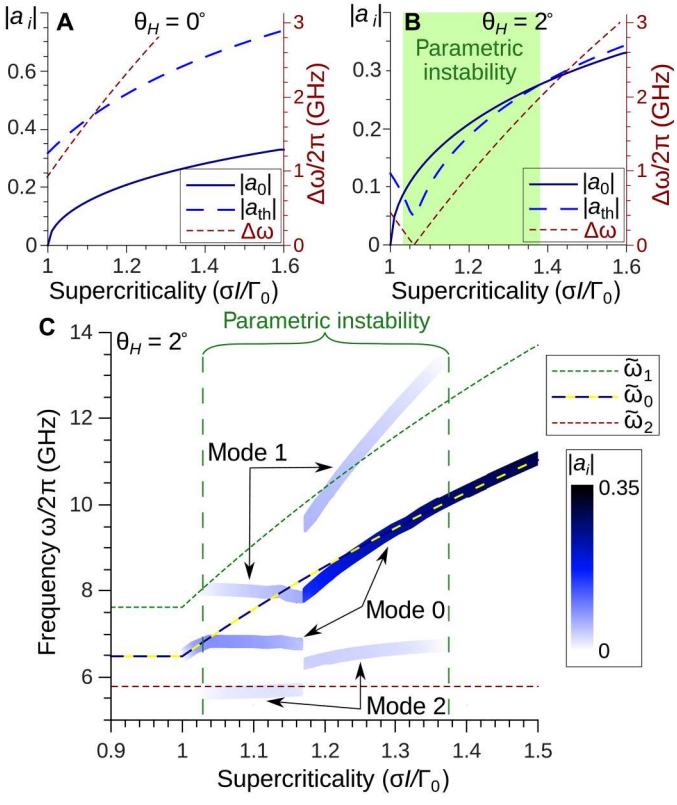

Fig. 4. Parametric interactions and mode dynamics in STNO. (**A** and **B**) Free-running amplitude a_0 of the mode 0 in the absence of parametric coupling, threshold of the parametric instability a_{th} (both, left axis), and detuning from parametric resonance condition Δω (right axis) in the case of perpendicular (A) and tilted (B) field. (**C**) Current dependence of stationary frequency and amplitude (color-coded) of the interacting modes, obtained as numerical integration of model Eq. 1 for $\theta_H = 2°$; dashed lines show free-running frequency $\tilde{\omega}_0$ and eigenfrequencies $\tilde{\omega}_1$ and $\tilde{\omega}_2$, which would be observed without parametric coupling.

DISCUSSION

The model results overall align closely with experimental observations. The finite range of multimode generation, the small (vanishing) frequency slope, the almost constant oscillation amplitude in the multimode regime, and the frequency jump are all observed in experiment. There is a quantitative difference in mode oscillation frequencies, which is on account of (i) the approximate calculation of nonlinear coefficients, particularly the phenomenological coefficient of nonlinear damping, and (ii) neglecting of the Oersted fields in the model that, according to experimental measurements below the threshold, result in the mode frequency increase about 70 MHz/mA, almost the same for different modes.

Our experiments have identified a regime of simultaneous multimode microwave emission in a nanopillar-based STNO. The physical process behind this is a second-order parametric instability between a pair of radially symmetric magnon modes and a pair of opposite azimuthal index modes, without any spatiotemporal overlap. The process, however, satisfies the constraint of both angular momentum and energy conservation through the hybridization of eigenmodes between the thin and the thick layers. This cogeneration has the additional feature of being incommensurable. The splitting between modes can thus be tuned by changing the characteristics of the nanopillar such as its diameter.

A future work direction will be to exploit nonuniform magnetic textures as a means to control continuously the splitting by an external bias parameter, such as the magnetic field. A particularly promising candidate is the vortex, where the splitting between the $\ell = \pm 1$ has been shown to vary strongly as a function of magnetic field. Given these findings, it is evident that the concurrent self-generation of diverse frequencies in dc-driven spintronic devices holds substantial promise. This has implications for neuromorphic and

wave-based approaches, especially when considering potential applications that use frequency multiplexing techniques.

METHODS

Device fabrication

The spin transfer nano-oscillator device used in this investigation consists of a permalloy $Ni_{80}Fe_{20}$ bilayer separated by a 10-nm copper (Cu) spacer, deposited on a silicon (Si) wafer. The permalloy layers are 4 and 15 nm in thickness. We fabricated the device with a diameter of 250 nm using established e-beam lithography and ion milling techniques, following the design and methodology outlined in detail in (*36*).

Microwave measurements

All microwave electrical measurements were carried out at room temperature using the circuit represented in Fig. 1A. The sample is mounted at a fixed sample holder between the pole pieces of an electromagnet producing a uniform magnetic field. A dc current flows through the device, and the ac component is extracted via a bias-T. This is then amplified and analyzed using an Agilent spectrum analyzer operating up to 26.5 GHz and a low-noise preamplifier (32-dB gain, 1.9-dB noise figure, 4- to 20-GHz range).

Micromagnetic simulations

The micromagnetic simulations were performed by the graphics processing unit (GPU)-accelerated simulation software Fastmag (*35*). In all the micromagnetic simulations, we use the following material parameters, which were experimentally determined from the passive STNO dynamics (*36*): saturation magnetization of the thin layer $\mu_0 M_{s,\mathrm{thin}} = 0.82$ T and of the thick layer $\mu_0 M_{s,\mathrm{thick}} = 0.96$ T; Gilbert damping parameters $\alpha_{G,\mathrm{thin}} = 0.015$ and $\alpha_{G,\mathrm{thick}} = 0.0085$, respectively, gyromagnetic ratio $\gamma = 1.87 \times 10^{11}\ \mathrm{s^{-1}T^{-1}}$, and exchange stiffness $A = 10.5$ pJ/m are identical in both layers; spin-polarization efficiency $\varepsilon = 0.3$ (*34*). In the simulations of active STNO dynamics, we account for mutual STT in both layers and the effect of Oersted fields. A tetrahedral volume mesh with a resolution of 2.6 nm, which is smaller than the exchange length of Py, is used. The simulation runs for a total duration of 120 ns; however, only the last 60 ns are subjected to postprocessing. The output information includes the magnetization (M) as a function of spatial coordinates (x, y, and z) and time (t). Simulations of linear spin wave eigenmodes, presented in Fig. 3, were performed at zero dc current and, consequently, zero Oersted fields. A microwave magnetic field $\boldsymbol{b} = b_{rf}\boldsymbol{e}_y$ was applied in one quarter of the pillar, and the dynamic magnetization was also recorded in a quarter, so that azimuthal modes $\ell = \pm 1, \pm 2,$ (except for the modes with azimuthal numbers $l = \pm 4, \pm 8, \ldots$) become visible.

Calculation of parameters for the analytical model

Linear frequencies for the model Eq. 1 were extracted from micromagnetic data. They are equal to $\omega_0/2\pi = 6.32$ GHz, $\omega_1/2\pi = 7.36$ GHz, and $\omega_2/2\pi = 4.48$ GHz for the case of perpendicular field and $\omega_0/2\pi = 6.48$ GHz, $\omega_1/2\pi = 7.62$ GHz, and $\omega_2/2\pi = 5.78$ GHz for $\theta_H = 2°$. Calculation of nonlinear parameters is a complex task. For spin wave eigenmodes in magnetic nanostructures, it can be solved using the recently developed vector Hamiltonian formalism for spin wave dynamics (*37*) and micromagnetically simulated mode profiles. Within this formalism, the four-magnon part of the Hamiltonian is given by

$$\mathcal{H}^{(4)} = \int \frac{\omega_M}{8V}\left(|\boldsymbol{s}|^2\boldsymbol{\mu}_0 \cdot \hat{\boldsymbol{N}} \cdot (|\boldsymbol{s}|^2\boldsymbol{\mu}_0) - |\boldsymbol{s}|^2\boldsymbol{s} \cdot \hat{\boldsymbol{N}} \cdot \boldsymbol{s}\right)d\boldsymbol{r} \tag{3}$$

where $\boldsymbol{\mu}_0$ is the static magnetization distribution, $\hat{\boldsymbol{N}}$ is the operator of magnetic self-interactions (exchange, dipolar, anisotropy, etc.), and integration goes over the whole sample volume V. Substituting dynamic magnetization $\boldsymbol{s}$ in the form of the eigenmodes sum $\boldsymbol{s} = \sum a_i\boldsymbol{s}_i$ + c.c., where a_i and $\boldsymbol{s}_i$ are mode amplitude and profile, respectively, one finds rather cumbersome equations for all four-magnon coefficients.

Yet, such calculations require very pure profiles of spin wave modes. In our case, the intermode distance is small, resulting in resonance peaks that overlap notably (see Fig. 3). Application of excitation field with specific profile (e.g., uniform, antisymmetric, circular, etc.) does not assist in the excitation of specific modes due to mode hybridization and complex static magnetization distribution, while utilization of drastically decreased damping leads to long simulation time. In addition, Oersted fields of dc current changes the static magnetization distribution and the mode structure to some extent, and rigorous consideration requires calculation of nonlinear coefficients at different dc currents.

For the abovementioned reasons, we made simple estimation of nonlinear coefficients instead of rigorous calculations. In our case of thin dots with perpendicular (or close to perpendicular) static magnetization, only two terms are dominant in the expression for nonlinear four-magnon coefficient

$$\begin{aligned} W_{12,34} \approx \tfrac{\omega_M}{2V}\int\{&(\boldsymbol{s}_1 \cdot \boldsymbol{s}_3^*)\boldsymbol{\mu}_0 \cdot \hat{\boldsymbol{N}} \cdot [(\boldsymbol{s}_2 \cdot \boldsymbol{s}_4^*)\boldsymbol{\mu}_0] \\ &+ (\boldsymbol{s}_1 \cdot \boldsymbol{s}_4^*)\boldsymbol{\mu}_0 \cdot \hat{\boldsymbol{N}} \cdot [(\boldsymbol{s}_2 \cdot \boldsymbol{s}_3^*)\boldsymbol{\mu}_0]\}d\boldsymbol{r} \end{aligned} \tag{4}$$

with magnetodipolar operator $\hat{\boldsymbol{N}} = \int d\boldsymbol{r}'\hat{\boldsymbol{G}}(\boldsymbol{r}, \boldsymbol{r}')$ expressed via magnetostatic Green function $\hat{\boldsymbol{G}}$. For the perpendicular field, we assume uniform static magnetization $\boldsymbol{\mu}_0 = \boldsymbol{e}_z$ and approximate mode profiles as $\boldsymbol{s} \sim (\boldsymbol{e}_x + i\boldsymbol{e}_y)J_m(k_{nm}r)e^{im\phi}$ with pinned boundary conditions at the dot edges and proper normalization (*37*). Thus, we get values $T_0/2\pi = 48$ GHz, $T_1 \approx T_2 \approx T_{01} \approx 2\pi \times 32$ GHz ($T_i \equiv W_{ii,ii}$, $T_{ij} \equiv W_{ij,ij}$), for the calculation of which full localization of mode 0, 1 (2) in the thin (thick) layer was assumed. When the field is weakly tilted, the considered major contribution changes proportionally to $\cos^2\theta_M$, where θ_M is the magnetization angle. This difference of about 3 to 5% is neglected. For the coefficient $W_{00,12}$, we assume that interaction takes place in the thin layer only, as modes 0 and 1 are mostly localized there. Then, this coefficient is proportional to the part of the dynamic magnetic moment of mode 2 in the thin layer, and we get $W_{00,12}/2\pi = 4$ GHz for $\theta_H = 0°$ and $W_{00,12}/2\pi = 13$ GHz in the tilted state. The contribution of interlayer magnetodipolar interaction is much smaller than the one within the thin layer and is neglected.

The nonlinear terms of the STT were calculated as follows. For a spatially uniform precession, the STT term is equal to $\sigma I(1 - |a|^2)a$ (*23*). The corresponding nonlinear term in energy is, thus, proportional to $|a|^4$. For spatially nonuniform dynamics, we substitute a with a sum of spin wave modes and average over the layer volume. Thus, we find the STT term equal to $\sigma_i I(1 - \tilde{\xi}_i|a_i|^2 - 2\sum_{j\neq i}\tilde{\xi}_{ij}|a_j|^2)$, where the nonlinear coefficients

are defined as

$$\tilde{\xi}_{ij} = \frac{\langle J^2_{m_i}(k_i r) J^2_{m_j}(k_j r)\rangle}{\langle J^2_{m_i}(k_i r)\rangle \langle J^2_{m_j}(k_j r)\rangle} \quad (5)$$

with $\langle f\rangle = (2/R^2)\int_0^R f(r) r dr$ being the spatial averaging. Thus, we get $\tilde{\xi}_0 = 2.1$, $\tilde{\xi}_1 = \xi_2 = 1.55$, and $\tilde{\xi}_{01} = 1.43$. The coefficients of nonlinear damping are more phenomenological (*23*) and cannot be calculated rigorously. For a circularly precessing macrospin, the damping is often accounted for as $\tilde{\Gamma} = \Gamma_0(1 + |a|^2)$, i.e., with the same nonlinear term as STT. Thus, we simply assume $\xi = \tilde{\xi}$.

The STT efficiency for mode 2, which is different from the ones of modes 0 and 1 due to the localization of this mode in both layers, is calculated in a straightforward manner

$$\frac{\sigma_2}{\sigma} = \frac{(1-\beta^2)t_1}{t_1 + \beta^2 t_2} \quad (6)$$

where t_1 (t_2) is the thickness of thin (thick) layer, and β is the ratio of dynamic magnetization in thick layer to the one in thin layer. Using this expression, we get $\sigma_2 = -0.16\sigma$ for $\theta_H = 0°$ and $\sigma_2 = 0.4\sigma$ for $\theta_H = 2°$.

Supplementary Materials

This PDF file includes:

Supplementary Text
Figs. S1 to S3

REFERENCES AND NOTES

1. J. C. Slonczewski, Current-driven excitation of magnetic multilayers. *J. Magn. Magn. Mater.* **159**, L1–L7 (1996).
2. L. Berger, Emission of spin waves by a magnetic multilayer traversed by a current. *Phys. Rev. B* **54**, 9353–9358 (1996).
3. S. Wolf, D. Awschalom, R. Buhrman, J. M. Daughton, S. von Molnár, M. Roukes, A. Y. Chtchelkanova, D. Treger, Spintronics: A spin-based electronics vision for the future. *Science* **294**, 1488–1495 (2001).
4. L. Thomas, G. Jan, J. Zhu, H. Liu, Y.-J. Lee, S. Le, R.-Y. Tong, K. Pi, Y.-J. Wang, D. Shen, R. He, J. Haq, J. Teng, V. Lam, K. Huang, T. Zhong, T. Torng, P.-K. Wang, Perpendicular spin transfer torque magnetic random access memories with high spin torque efficiency and thermal stability for embedded applications (invited). *J. Appl. Phys.* **115**, 172615 (2014).
5. A. Hirohata, K. Yamada, Y. Nakatani, I.-L. Prejbeanu, B. Diény, P. Pirro, B. Hillebrands, Review on spintronics: Principles and device applications. *J. Magn. Magn. Mater.* **509**, 166711 (2020).
6. S. I. Kiselev, J. C. Sankey, I. N. Krivorotov, N. C. Emley, R. J. Schoelkopf, R. A. Buhrman, D. C. Ralph, Microwave oscillations of a nanomagnet driven by a spinpolarized current. *Nature* **425**, 380–383 (2003).
7. Q. Mistral, J.-V. Kim, T. Devolder, P. Crozat, C. Chappert, J. A. Katine, M. J. Carey, K. Ito, Current-driven microwave oscillations in current perpendicular-to-plane spin-valve nanopillars. *Appl. Phys. Lett.* **88**, 192507 (2006).
8. D. Houssameddine, S. Florez, J. Katine, J.-P. Michel, U. Ebels, D. Mauri, O. Ozatay, B. Delaet, B. Viala, L. Folks, B. D. Terris, M.-C. Cyrille, Spin transfer induced coherent microwave emission with large power from nanoscale MgO tunnel junctions. *Appl. Phys. Lett.* **93**, 022505 (2008).
9. Q. Mistral, M. van Kampen, G. Hrkac, J.-V. Kim, T. Devolder, P. Crozat, C. Chappert, L. Lagae, T. Schrefl, Current-driven vortex oscillations in metallic nanocontacts. *Phys. Rev. Lett.* **100**, 257201 (2008).
10. Z. Zeng, G. Finocchio, H. Jiang, Spin transfer nano-oscillators. *Nanoscale* **5**, 2219–2231 (2013).
11. R. Tomasello, R. Verba, V. Lopez-Dominguez, F. Garesci, M. Carpentieri, M. Di Ventra, P. K. Amiri, G. Finocchio, Antiferromagnetic parametric resonance driven by voltage-controlled magnetic anisotropy. *Phys Rev Appl* **17**, 034004 (2022).
12. S. Bonetti, P. Muduli, F. Mancoff, J. Åkerman, Spin torque oscillator frequency versus magnetic field angle: The prospect of operation beyond 65 GHz. *Appl. Phys. Lett.* **94**, 102507 (2009).
13. O. V. Prokopenko, E. Bankowski, T. Meitzler, V. S. Tiberkevich, A. N. Slavin, Influence of temperature on the performance of a spin-torque microwave detector. *IEEE Trans. Magn.* **48**, 3807–3810 (2012).
14. W. H. Rippard, M. R. Pufall, S. Kaka, S. E. Russek, T. J. Silva, Direct-current induced dynamics in $Co_{90}Fe_{10}/Ni_{80}Fe_{20}$ point contacts. *Phys. Rev. Lett.* **92**, 027201 (2004).
15. E. Grimaldi, R. Lebrun, A. Jenkins, A. Dussaux, J. Grollier, V. Cros, A. Fert, H. Kubota, K. Yakushiji, A. Fukushima, R. Matsumoto, S. Yuasa, G. Cibiel, P. Bortolotti, G. Pillet, Spintronic nano-oscillators: Towards nanoscale and tunable frequency devices, in *Proceedings of the 2014 IEEE International Frequency Control Symposium (FCS)*, Taipei, Taiwan, 19–22 May 2014, pp. 1–6.
16. S. Louis, V. Tyberkevych, J. Li, I. Lisenkov, R. Khymyn, E. Bankowski, T. Meitzler, I. Krivorotov, A. Slavin, Low power microwave signal detection with a spin-torque nano-oscillator in the active self-oscillating regime. *IEEE Trans. Magn.* **53**, 1–4 (2017).
17. A. Litvinenko, V. Iurchuk, P. Sethi, S. Louis, V. Tyberkevych, J. Li, A. Jenkins, R. Ferreira, B. Dieny, A. Slavin, U. Ebels, Ultrafast sweep-tuned spectrum analyzer with temporal resolution based on a spin-torque nano-oscillator. *Nano Lett.* **20**, 6104–6111 (2020).
18. W. Skowroński, J. ChĘciński, S. ZiĘtek, K. Yakushiji, S. Yuasa, Microwave magnetic field modulation of spin torque oscillator based on perpendicular magnetic tunnel junctions. *Sci. Rep.* **9**, 19091 (2019).
19. M. Madami, S. Bonetti, G. Consolo, S. Tacchi, G. Carlotti, G. Gubbiotti, F. Mancoff, M. A. Yar, J. Åkerman, Direct observation of a propagating spin wave induced by spin-transfer torque. *Nat. Nanotechnol.* **6**, 635–638 (2011).
20. J. Torrejon, M. Riou, F. A. Araujo, S. Tsunegi, G. Khalsa, D. Querlioz, P. Bortolotti, V. Cros, K. Yakushiji, A. Fukushima, H. Kubota, S. Yuasa, M. D. Stiles, J. Grollier, Neuromorphic computing with nanoscale spintronic oscillators. *Nature* **547**, 428–431 (2017).
21. J. Grollier, D. Querlioz, M. D. Stiles, Spintronic nanodevices for bioinspired computing. *Proc. IEEE* **104**, 2024–2039 (2016).
22. M. Riou, J. Torrejon, B. Garitaine, F. Abreu Araujo, P. Bortolotti, V. Cros, S. Tsunegi, K. Yakushiji, A. Fukushima, H. Kubota, S. Yuasa, D. Querlioz, M. D. Stiles, J. Grollier, Temporal pattern recognition with delayed-feedback spin-torque nano-oscillators. *Phys. Rev. Appl.* **12**, 024049 (2019).
23. A. Slavin, V. Tiberkevich, Nonlinear auto-oscillator theory of microwave generation by spin-polarized current. *IEEE Trans. Magn.* **45**, 1875–1918 (2009).
24. A. J. Eklund, S. R. Sani, S. M. Mohseni, J. Persson, B. G. Malm, J. Åkerman, Triple mode-jumping in a spin torque oscillator. *Proceedings of the 2013 22nd International Conference on Noise and Fluctuations (ICNF)*, Montpellier, France, 24–28 June 2013, pp. 1–4.
25. O. G. Heinonen, P. K. Muduli, E. Iacocca, J. Akerman, Decoherence, mode hopping, and mode coupling in spin torque oscillators. *IEEE Trans. Magn.* **49**, 4398–4404 (2013).
26. E. Iacocca, O. Heinonen, P. K. Muduli, J. Åkerman, Generation linewidth of mode-hopping spin torque oscillators. *Phys. Rev. B* **89**, 054402 (2014).
27. D. V. Slobodianiuk, Transition from one- to two-mode generation regime in STNO mediated by thermal noise. *Condens. Matter Phys.* **17**, 13801 (2014).
28. L. Chen, W. Wang, X. Zhan, K. Zhou, Z. Gao, L. Liang, T. Zhou, Y. Du, R. Liu, Spatial coexistence of multiple modes in a nanogap spin Hall nano-oscillator with extended Pt/Ni/Fe trilayers. *Phys. Rev. B* **105**, 104413 (2022).
29. L. Yang, R. Verba, V. Tiberkevich, T. Schneider, A. Smith, Z. Duan, B. Youngblood, K. Lenz, J. Lindner, A. N. Slavin, I. N. Krivorotov, Reduction of phase noise in nanowire spin orbit torque oscillators. *Sci. Rep.* **5**, 16942 (2015).
30. V. S. L'vov, *Wave Turbulence under Parametric Excitation* (Springer-Verlag, New York, 1994).
31. H. Suhl, The theory of ferromagnetic resonance at high signal powers. *J. Phys. Chem. Solid* **1**, 209–227 (1957).
32. P. Pirro, V. I. Vasyuchka, A. A. Serga, B. Hillebrands, Advances in coherent magnonics. *Nat. Rev. Mater.* **6**, 1114–1135 (2021).
33. P. Pirro, T. Sebastian, T. Brächer, A. A. Serga, T. Kubota, H. Naganuma, M. Oogane, Y. Ando, B. Hillebrands, Non-gilbert-damping mechanism in a ferromagnetic heusler compound probed by nonlinear spin dynamics. *Phys. Rev. Lett.* **113**, 227601 (2014).
34. A. Hamadeh, G. De Loubens, V. Naletov, J. Grollier, C. Ulysse, V. Cros, O. Klein, Autonomous and forced dynamics in a spin-transfer nano-oscillator: Quantitative magnetic-resonance force microscopy. *Phys. Rev. B* **85**, 140408 (2012).
35. R. Chang, S. Li, M. V. Lubarda, B. Livshitz, V. Lomakin, FastMag: Fast micromagnetic simulator for complex magnetic structures (invited). *J. Appl. Phys.* **109**, 07D358 (2011).
36. V. V. Naletov, G. De Loubens, G. Albuquerque, S. Borlenghi, V. Cros, G. Faini, J. Grollier, H. Hurdequint, N. Locatelli, B. Pigeau, A. N. Slavin, V. S. Tiberkevich, C. Ulysse, T. Valet, O. Klein, Identification and selection rules of the spin-wave eigenmodes in a normally magnetized nanopillar. *Phys. Rev. B* **84**, 224423 (2011).

37. V. Tyberkevych, A. Slavin, P. Artemchuk, G. Rowlands, *Vector Hamiltonian Formalism for Nonlinear Magnetization Dynamics* (2020); arXiv:2011.13562 [cond-mat.mtrl-sci].
38. R. Verba, L. Körber, K. Schultheiss, H. Schultheiss, V. Tiberkevich, A. Slavin, Theory of three-magnon interaction in a vortex-state magnetic nanodot. *Phys. Rev. B* **103**, 014413 (2021).

Acknowledgments
Funding: This work was supported by the European Research Council within the Starting grant no. 101042439 "CoSpiN"; the Deutsche Forschungsgemeinschaft (DFG, German Research Foundation)-TRR 173-268565370 (project B01); the Agence Nationale de la Recherche (ANR) under grant nos. ANR-20-CE24-0012 "Marin" and ANR-21-CE24-0031 "Harmony"; the EU-project H2020-2020-FETOPEN k-NET-899646; the EU-project HORIZON-EIC-2021-PATHFINDEROPEN PALANTIRI-101046630; the National Academy of Sciences of Ukraine, project no. 0122U002462; and the project PRIN 2020LWPKH7 funded by the Italian Ministry of University and Research. **Author contributions:** A.A.H. and G.D.L. performed and analyzed the measurements with support from O.K. A.A.H. and V.B. carried out micromagnetic simulations with support from P.P. D.S., G.M., and R.V. developed the analytical theory, and D.S. performed the theoretical calculations. R.M., G.F., V.L., and M.M. discussed the numerical simulations. A.A. H., G.D.L., P.P., and O.K. led this project. A.A.H. and R.V. wrote the manuscript with the help of all the coauthors. All authors contributed to the scientific discussion and commented on the manuscript. **Competing interests:** The authors declare that they have no competing interests. **Data and materials availability:** All data needed to evaluate the conclusions in the paper are present in the paper and/or the Supplementary Materials.

Submitted 5 August 2023
Accepted 14 November 2023
Published 13 December 2023
10.1126/sciadv.adk1430